Dissipation and enstrophy in isotropic turbulence: Resolution effects and scaling in direct numerical simulations

D. A. Donzis, P. K. Yeung, and K. R. Sreenivasan

Citation: Physics of Fluids **20**, 045108 (2008); doi: 10.1063/1.2907227
View online: http://dx.doi.org/10.1063/1.2907227
View Table of Contents: http://scitation.aip.org/content/aip/journal/pof2/20/4?ver=pdfcov
Published by the AIP Publishing

Dissipation and enstrophy in isotropic turbulence: Resolution effects and scaling in direct numerical simulations

D. A. Donzis,[1,2] P. K. Yeung,[1,a)] and K. R. Sreenivasan[2,3]
[1]*School of Aerospace Engineering, Georgia Institute of Technology, Atlanta, Georgia 30332, USA*
[2]*Institute for Physical Science and Technology, University of Maryland, College Park, Maryland 20742, USA*
[3]*International Centre for Theoretical Physics, Strada Costiera 11, 34014 Trieste, Italy*

(Received 29 October 2007; accepted 4 March 2008; published online 30 April 2008)

Existing experimental and numerical data suggest that the turbulence energy dissipation and enstrophy (i.e., the square of vorticity) possess different scaling properties, while available theory suggests that there should be no differences at sufficiently high Reynolds numbers. We have performed a series of direct numerical simulations with up to 2048^3 grid points where advanced computational power is used to increase the Reynolds number (up to 650 on the Taylor scale) or to resolve the small scales better (down to 1/4 of a Kolmogorov scale). Our primary goal is to assess the differences and similarities between dissipation and enstrophy. Special attention is paid to the effects of small-scale resolution on the quality and reliability of the data, in view of recent theoretical work [V. Yakhot and K. R. Sreenivasan, "Anomalous scaling of structure functions and dynamic constraints on turbulence simulations," J. Stat. Phys. **121**, 823 (2005)] which stipulates the resolution needed to obtain a moment of a given order. We also provide error estimates as a function of small-scale resolution. Probability density functions of dissipation and enstrophy at high Reynolds number reveal the presence of extreme events several thousands times of the mean. The extreme events in dissipation and enstrophy fields appear to scale alike, substantially overlap in space, and are nearly statistically isotropic, while fluctuations of moderate amplitudes, at least for the present Reynolds numbers, show persistent differences. Conditional sampling shows that intense dissipation is likely to be accompanied by similarly intense enstrophy, but intense enstrophy is not always accompanied by intense dissipation. © *2008 American Institute of Physics*.
[DOI: 10.1063/1.2907227]

I. INTRODUCTION

The energy dissipation rate (ϵ) and enstrophy (Ω, squared vorticity) represent, respectively, the intensity of local straining and rotation of turbulence, and are both important descriptors of small-scale motion. In homogeneous turbulence, ϵ and $\nu\Omega$ (where ν is the kinematic viscosity) have the same average value, which is also nearly true in regions of approximate homogeneity such as the inertial sublayers in wall-bounded flows. However, other moments may differ. Indeed, almost all sources of available data (e.g., Refs. 1–10) suggest that enstrophy is more intermittent or exhibits more intensely localized fluctuations. Specifically, in both simulation and experiment, local averages of enstrophy, taken over subdomains in the inertial range, possess probability density functions (PDFs) that exhibit a greater propensity, as the subdomain volume decreases, for wider tails than similarly averaged dissipation; the corresponding intermittency exponent is also larger for enstrophy. In contrast, plausible theoretical arguments[11–13] as well as a recent model of velocity gradient evolution[14] have advanced the view that these differences arise from the low Reynolds numbers considered and that they would vanish at higher Reynolds numbers. This issue is worthy of attention, at least to avoid ambiguities in the choice of the variable used to represent small scales[15] and to clarify the roles of local straining and rotation in the modeling of turbulent dispersion.[16] Recent advances in computing power have made possible direct numerical simulations (DNS) of homogeneous turbulence at Reynolds numbers large enough to clarify the question above. The principal theme of the present paper is to analyze data from such simulations, giving detailed and careful consideration to the effects of finite grid resolution.

Obviously, our general interest is to achieve the highest possible Reynolds numbers by taking advantage of the most powerful computers available. If we aim at resolving the small scales to within a constant multiple α_1 of the Kolmogorov scale η and use a computational box whose linear size is a multiple α_2 of the integral length scale, $\mathcal{L}$, then one can relate the Reynolds number (Re or R_λ, based on the integral or the Taylor scale, respectively) and the number of grid points (N in each direction) to the computational work required. The first relation of interest is

$$N \approx \frac{\alpha_2}{\alpha_1}\left(\frac{\mathcal{L}}{\eta}\right) \approx 0.4\left(\frac{\alpha_2}{\alpha_1}\right)\mathrm{Re}^{3/4} \approx 0.052\frac{\alpha_2}{\alpha_1}R_\lambda^{3/2}, \qquad (1)$$

where we have used standard local isotropy relations and the phenomenological result[17,18] in DNS that $\langle\epsilon\rangle \approx 0.4u'^3/\mathcal{L}$; here u' is the root-mean-square (rms) velocity and the integral scale $\mathcal{L}$ is defined from the energy spectrum $E(k)$ as

a)Electronic mail: pk.yeung@ae.gatech.edu.

TABLE I. DNS parameters: Taylor-scale Reynolds number $R_\lambda = u'\lambda/\nu$, number of grid points N^3, viscosity ν, resolution expressed in $k_{\max}\eta$ and $\Delta x/\eta$, mean energy dissipation rate $\langle\epsilon\rangle$ (equal to $\nu\langle\Omega\rangle$), number of instantaneous snapshots (N_r) processed as independent realizations, and simulation time period T normalized by eddy-turnover time T_E ($\mathcal{L}/u'$).

R_λ	140	140	140	140	240	240	240	390	390	650
N^3	256^3	512^3	1024^3	2048^3	512^3	1024^3	2048^3	1024^3	2048^3	2048^3
ν (10^{-3})	2.8	2.8	2.8	2.8	1.1	1.1	1.1	0.437	0.437	0.1732
$k_{\max}\eta$	1.41	2.82	5.72	11.15	1.42	2.84	5.35	1.37	2.77	1.39
$\Delta x/\eta$	2.10	1.05	0.52	0.27	2.08	1.04	0.55	2.15	1.07	2.12
$\langle\epsilon\rangle$	1.18	1.22	1.14	1.25	1.14	1.12	1.42	1.28	1.24	1.23
N_r	11	16	18	11	13	12	14	16	21	15
T/T_E	10.0	7.2	8.5	6.0	9.4	5.4	5.4	6.9	3.7	6.2

$$\mathcal{L} = \frac{\pi}{2u'^2}\int_0^\infty \frac{E(k)}{k}dk. \tag{2}$$

The second relation to immediately follow arises from the fact that the computational work varies as N^3M (to within $\ln_2 N$ for Fourier pseudospectral methods), where M is the number of time steps needed for reliable averaging over a period of time (T) in a stationary state. Assuming that the latter is at least five eddy-turnover times ($T_E=\mathcal{L}/u'$), and using a Courant number of about 0.5, we have

$$W \approx \frac{10}{(\alpha_1/\alpha_2)^4}\left(\frac{\mathcal{L}}{\eta}\right)^4 \propto \frac{R_\lambda^6}{(\alpha_1/\alpha_2)^4}. \tag{3}$$

While the coefficients in the equations above are not precise, it is clear that the computational work increases with grid refinement according to the fourth power of the resolution: resolving $\eta/2$ takes $4^4=256$ times more CPU effort than resolving 2η. In most published work aimed at reaching highest possible Reynolds numbers α_1 is about 2, while α_2 is about 5 (see, e.g., Refs. 19–23). This "standard" resolution is usually adequate for computing second-order quantities such as the energy spectrum $E(k)$ (because it falls off rapidly for wavenumbers $k>1/\eta$), but is known to underestimate high-order moments of velocity gradients, hence of energy dissipation rate, and enstrophy. Recognition of the dynamical significance of scales smaller than η (e.g., in reacting flows[24]) has led to recent theoretical work[25–27] which shows that a stricter resolution criterion than commonly practiced must be adopted for capturing all relevant scales. In particular, Yakhot and Sreenivasan[25] proposed that the finest scale that needs to be resolved varies as $\eta \mathrm{Re}^{-1/4}$, which poses increasing difficulties as the Reynolds number increases. While this stringent requirement may not be mandatory when our goals are limited to getting second-order moments to within a specified accuracy, it is important to assess, in the light of the considerations stated above, the degree to which the conclusions from simulation of more modest resolution remain valid for high-order moments. The most direct test is to compare simulations at the same Reynolds number but different degrees of resolution.[10,27–29]

Thus, we have two main objectives for this paper. First, we examine resolution effects on the statistics of dissipation and enstrophy as well as velocity gradients. Second, we obtain a new understanding of the Reynolds number scaling of ϵ and Ω using a DNS database[9] for R_λ up to about 650, with due recognition of resolution effects and extreme fluctuations; in particular, we discuss similarities and differences between ϵ and Ω. For these purposes, simulations of up to 2048^3 in size have been performed using a massively parallel implementation of the pseudospectral algorithm of Rogallo,[30] for which the highest resolvable wavenumber is given by $k_{\max}=\sqrt{2}N/3$. For a domain of linear size 2π the grid spacing Δx is simply $2\pi/N$ so that

$$\frac{\Delta x}{\eta} = \frac{\sqrt{2}}{3}\frac{2\pi}{k_{\max}\eta} \approx \frac{2.96}{k_{\max}\eta}, \tag{4}$$

which relates the resolution parameter $k_{\max}\eta$ to the grid spacing. The time stepping is second-order Runge–Kutta and the viscous term is exactly treated via an integrating factor.[30] Aliasing errors are carefully controlled by a combination of truncation and phase shifting techniques. The turbulence is maintained stationary by stochastic forcing at large scales.[19] Table I provides a listing of the basic parameters of simulations, including those where increasing computational power was used for resolving small scales better instead of increasing the Reynolds number. The best small-scale resolution achieved ($k_{\max}\eta \approx 11$, at $R_\lambda \approx 140$) is similar to that in a new study[31] of strain rate and vorticity alignment where such resolution is shown to make more rigorous results possible. Ensemble averaging over a number (N_r) of instantaneous snapshots of archived velocity fields is taken in the same manner as in past publications.[18,32,33] Our present focus on strong but short-lived events at small scales allows us to take realizations closer in time than otherwise, without compromising the desired statistical independence among different datasets. Nevertheless, since samples of the most intense fluctuations are inherently few in number, a clear distinction between errors or uncertainties due to finite resolution and finite sampling is not always possible.

The results to be presented show that there is a systematic need for finer grid resolution as the order of the moment of small-scale properties, or the Reynolds number, increases. Traditional resolution of $\Delta x \approx 2\eta$ is adequate for accurate results in the mean values of ϵ and Ω, but not for high-order moments or for mean squares of second derivatives of the velocity. In Sec. II we examine the data at $R_\lambda \approx 140$ and 240 over a range of grid resolutions and conclude that an acceptable resolution for fourth-order moments at these Reynolds

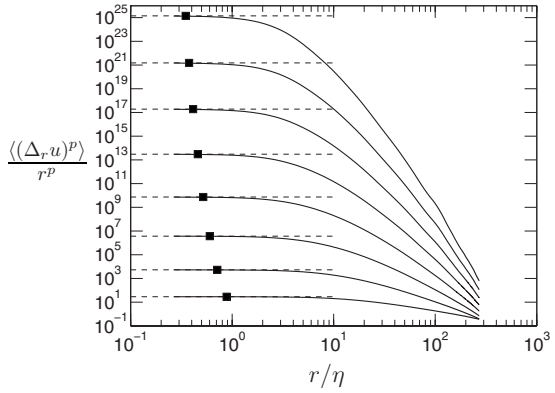

FIG. 1. Scaling of even-order longitudinal structure functions $\langle(\Delta_r u)^p\rangle/r^p$ for $p=2$, 4, 6, 8, 10, 12, 14, and 16 (bottom to top), from a highly resolved simulation at $R_\lambda \approx 140$ (2048^3, $k_{\max}\eta \approx 11.2$, $\Delta x/\eta \approx 1/4$). The horizontal dashed lines indicate limits of analytic range behavior. Solid squares denote η_p/η [Eq. (6)] as proposed by Yakhot and Sreenivasan (Ref. 25).

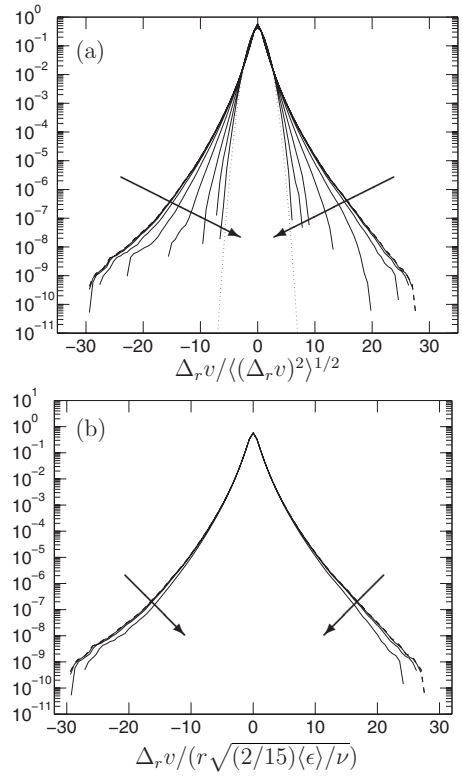

FIG. 2. PDFs of transverse velocity increments in different normalizations (as written under the coordinate axes), from the same highly resolved $R_\lambda \approx 140$ simulation as in Fig. 1, with arrows in the direction of increasing scale size r. The dashed lines correspond to the smallest scale available in the simulation ($r/\eta \approx 1/4$, which almost coincides to data at $r/\eta \approx 1/2$). In (a) we show data for $r/\Delta x=1$, 2, 4, 8, 16, 32, 64, 128, and 256 and a standard Gaussian (dotted curve) for comparison. In (b) we show data at the four smallest r, i.e., $r/\Delta x=1$, 2, 4, and 8 ($r/\eta \approx 1/4$, 1/2, 1, and 2, with $k_{\max}\eta \approx 11$).

numbers is $k_{\max}\eta \approx 3$ or, according to Eq. (4), $\Delta x/\eta \approx 1$. We use a Taylor-series approach to develop an estimate of the error incurred with coarser resolutions and compare the requirements with recent theory.[25] In Sec. III we investigate whether dissipation and enstrophy statistics tend to scale similarly as the Reynolds number increases. The PDFs of ϵ and Ω are found to almost coincide in the range of fluctuations as large as a few thousand times the mean. Conditional sampling used in conjunction with decompositions of ϵ and Ω into the longitudinal, transverse, and cross-term contributions suggests that extreme events tend to occur close to each other in space, and the relative sizes of contributions from longitudinal and transverse velocity gradients are consistent with statistical isotropy. A summary of conclusions is given in Sec. IV. The Appendix contains a short derivation relevant to Sec. III, based on fourth-order isotropic tensor properties in incompressible turbulence.

II. EFFECTS OF RESOLUTION

A. The DNS data

A basic diagnostic of resolution effects is the behavior of the longitudinal velocity increments $\Delta_r u$ as the spatial separation approaches the smallest value allowed in a simulation (which is the grid spacing Δx). Figure 1 shows the longitudinal structure functions, or the moments $\langle(\Delta_r u)^p\rangle$, for increasing even orders p, from $p=2$ to 16, from a simulation at $R_\lambda \approx 140$, which at $k_{\max}\eta \approx 11.2$ ($\Delta x/\eta \approx 1/4$, on a 2048^3 grid) resolves down to a scale that is about an eighth of that used in standard practice. (Solid-square symbols are from the theory of Ref. 25, to be discussed below.) The structure functions are divided by r^p, such that analytic behavior is indicated by asymptotic plateaus corresponding to $\langle(\partial u/\partial x)^p\rangle$ (shown by dashed horizontal lines, computed using the finest resolution in Table I) in the limit of vanishing r. As expected, the minimum r/η needed to observe such behavior decreases with increasing the order p. It is clear that the analytic behavior for orders of 8 and upward requires resolution of sub-Kolmogorov scales [$\Delta x < \eta$ or $k_{\max}\eta > 3$, see Eq. (3)].

In addition to moments of different orders, it is also useful to examine the tails of the PDF of velocity increments over a range of scale sizes. Transverse gradients provide a stricter test: if they are adequately resolved, the longitudinal gradients are also expected to be satisfactorily resolved (in fact, slightly better). Figures 2(a) and 2(b) show such data for transverse increments from the same simulation as in Fig. 1, under two different normalizations. In (a) we have normalized velocity increments by their rms values and show the standardized PDFs over a wide range of r. It is clear that the increment at small r is highly non-Gaussian with wide tails, while at large r the increment becomes the difference between two independent, Gaussian random variables and hence Gaussian. On the other hand, for a resolution check (at relatively small values of r), it is useful to normalize $\Delta_r v$ by the product of r and the rms of transverse velocity gradients, i.e., $\sqrt{(2/15)\langle\epsilon\rangle/\nu}$. In this normalization, shown in Fig. 2(b), the PDFs should converge for r in the analytic range. It can be seen that results for $r/\eta \approx 2$ are significantly different from those at other values of r/η (≈ 1, 1/2, and 1/4). This figure confirms that, for this Reynolds number, the standard resolution of $k_{\max}\eta \approx 1.5$ is inadequate for the tails of the velocity gradient PDF, while the results with the resolution of $k_{\max}\eta \approx 3$ (or $\Delta x/\eta \approx 1$) converge reasonably well to those of smaller $\Delta x/\eta$.

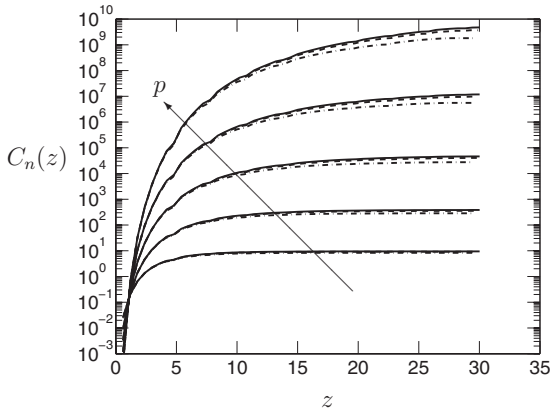

FIG. 3. Convergence test of contributions to moments of $z=\Delta_r v/(r\sqrt{(2/15)\langle\epsilon\rangle/\nu})$ through $C_p(z)$ [see Eq. (5)] at $r/\eta\approx 1/4$ (solid line), 1 (dashed line), and 2 (dash-dotted line), from the same highly resolved $R_\lambda\approx 140$ simulation as in Figs. 1 and 2. The arrow points in the direction of increasing p (4, 6, 8, 10, and 12).

The next test is one of statistical convergence. We note that statistical convergence alone without adequate resolution does not guarantee the accuracy of moments because the data could converge to incorrect quantities. For transverse increments which are statistically symmetric, we consider the quantity

$$C_p(z)=\int_{-z}^{z}(z')^p f(z')dz', \tag{5}$$

with z denotes the normalized velocity increment $\Delta_r v/(r\sqrt{(2/15)\langle\epsilon\rangle/\nu})$ and f as its PDF. By definition, $C_p(0)=0$, $C_p(\infty)=\langle(\Delta_r v/r)\rangle^p/(\sqrt{(2/15)\langle\epsilon\rangle/\nu})^p$ for any $p>0$. Figure 3 shows the data, for $p=4$, 6, 8, 10, and 12, and $r/\eta\approx 1/4$, 1, and 2 at $R_\lambda\approx 140$ from the same highly resolved simulation, as discussed in Figs. 1 and 2. [Data for $r/\eta\approx 1/2$ are, as in Fig. 2(b) above, indistinguishable from $r/\eta\approx 1/4$ and omitted for clarity.] Statistical convergence is indicated if the curves reach asymptotic values in the limit of large z. This convergence is attained reasonably well up to order of 8, but less so for higher orders and for smaller scales where stronger intermittency effects are present. By using local isotropy relations, we can show that in the limit of $r\ll\eta$ the value of $C_p(\infty)$ should be equal to $(2/15)^{p/2}\langle(\partial v/\partial x)^p\rangle/\langle(\partial v/\partial x)^2\rangle^{p/2}$, which strongly increases with p.

We also examine the accuracy of statistical results on dissipation and enstrophy. Recently, Yakhot and Sreenivasan[25] proposed a theory for the small scales, according to which the pth order moment of dissipation can be accurate only if the resolution is adequate to resolve analytic behavior in velocity structure functions of order $4p$. The connection between velocity differences and energy dissipation arises because the velocity gradients that contribute to dissipation can be regarded as the limits of appropriate velocity increments as the separation distance tends to zero. This requirement suggested in Ref. 25 differs from Kolmogorov's refined similarity hypothesis (K62),[34] which may be interpreted to require analytic ranges in moments of order $3p$. Furthermore, the theory implies that the smallest scale that needs to be resolved for the pth order structure function is

$$\eta_p/\eta\approx(R_\lambda^2/15)^{3/4+d_p}, \tag{6}$$

where $d_p=1/(\zeta_p-\zeta_{p+1}-1)$ and ζ_p is the inertial-range scaling exponent of structure functions of order p. The ratios η_p/η are included in Fig. 1 as solid squares which can be used to assess the adequacy of the resolution of our simulations according to Ref. 25. Note that to resolve all orders, i.e., as $p\to\infty$, the theory suggests that the smallest scale that needs to be captured is

$$\eta_{\min}\approx\mathcal{L}R_\lambda^{-2}. \tag{7}$$

This estimate, in fact, agrees with the multifractal prediction of the smallest relevant scale governed by the strongest singularities (see, e.g., Ref. 35).

A full comparison of the Yakhot–Sreenivasan theory and Kolmogorov refined similarity is not yet available, but preliminary tests in Ref. 27 mildly favor the former. If the former theory does prevail upon more rigorous examination, it is clear that we should view our fourth moment of dissipation with caution—since it would then require accurate structure functions of order of 16, which are rarely obtained in practice. Since both theoretical scenarios correspond to infinitely large Reynolds numbers and are conservative in this sense, we shall evaluate below dissipation moments up to order of 4 and independently assess their accuracy—thereby also contributing new information to the current discussion on resolution requirements.

In our simulations, the mean dissipation rate $\langle\epsilon\rangle$ (and also $\langle\Omega\rangle=\langle\epsilon\rangle/\nu$) are determined by the large scales that are subject to stochastic forcing and are insensitive to small-scale resolution. It is therefore convenient to normalize dissipation and enstrophy by their mean values, i.e., to define $\epsilon'\equiv\epsilon/\langle\epsilon\rangle$ and $\Omega'\equiv\Omega/\langle\Omega\rangle$ and to examine moments of these normalized quantities for orders $p\geq 2$. The moments $\langle(\epsilon')^p\rangle$ and $\langle(\Omega')^p\rangle$ for $p=2$, 3, and 4 are shown in Figs. 4(a) and 4(b) and Table II for different grid resolutions, with the Reynolds numbers kept nominally fixed at $R_\lambda\approx 140$ and 240 (see Table I). It is clear that finite resolution underestimates these moments, especially those at higher orders. However, differences among simulations with $k_{\max}\eta>3$ ($\Delta x/\eta<1$) appear to be within the 90% confidence intervals, and are, in any case, relatively small.

To check statistical convergence for the dissipation and enstrophy moments given above, we can examine the integrands $\epsilon'^p f_\epsilon(\epsilon')$ (and similarly for Ω), contributing to each moment of order p, where $f_\epsilon(\epsilon)$ is the PDF of ϵ. In Fig. 5 we show these integrands for $p=4$ at different resolutions with $R_\lambda\approx 140$. The area under each curve gives the normalized fourth-order moment, which is considered statistically converged if the curve falls to nearly zero in the limit of the largest sampled ϵ' and Ω'. This condition is met by all the curves shown, suggesting satisfactory convergence, yet the figure also clearly shows that the resolution $k_{\max}\eta\approx 1.41$ misses many samples of large ϵ' or Ω'. The inadequate resolution does not appear to affect samples of ϵ or Ω close to the mean: curves for dissipation and enstrophy show little

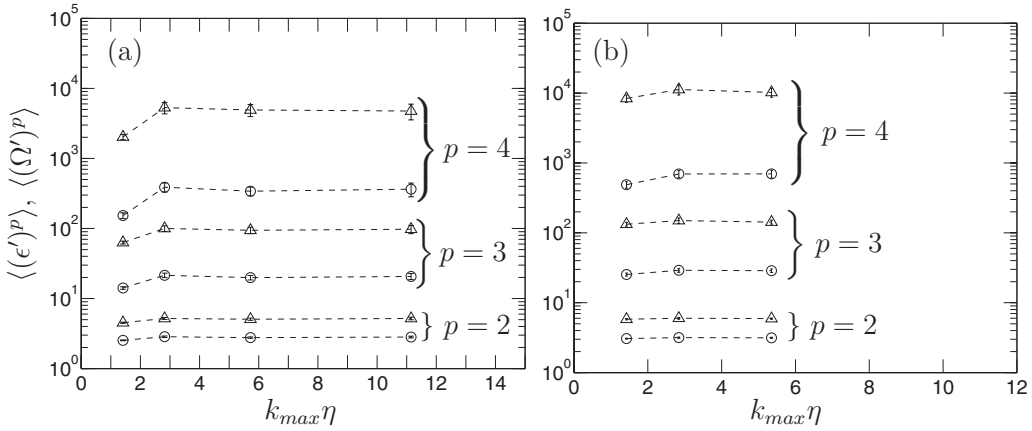

FIG. 4. Ensemble averaged moments of normalized dissipation rate and enstrophy: $\langle\epsilon'^p\rangle$ (○) and $\langle\Omega'^p\rangle$ (△) for orders $p=2$, 3, and 4 at different resolutions for (a) $R_\lambda\approx140$ and (b) $R_\lambda\approx240$, as listed in Table I. Vertical bars (partly hidden) indicate the extent of 90% confidence intervals.

difference for ϵ' up to about 7 and Ω' up to about 10, though both the location and the height of the peak are underestimated in simulations at resolution $k_{\max}\eta\approx1.41$.

It is of some interest to note from Table II that normalized moments of the form $\langle\epsilon^4\rangle/\langle\epsilon^2\rangle^2$ are less sensitive to resolution than "unnormalized" moments of the same order. This behavior can be understood by noting that some partial cancellation occurs in ratios of moments of orders close to each other. Another interpretation is that although finite resolution changes the shape of the dissipation and enstrophy PDFs by failing to capture the farthest tails, the actual PDFs obtained may—as will be seen in Sec. III—still retain the correct functional form, though with different values of parameters or coefficients involved.

TABLE II. Ensemble averaged moments of dissipation and enstrophy at $R_\lambda\approx140$ (top) and 240 (bottom) and different grid resolutions, with 90% confidence intervals.

		$R_\lambda\approx140$		
$k_{\max}\eta$	1.41	2.82	5.72	11.15
$\langle(\epsilon')^2\rangle$	2.53 ± 0.04	2.85 ± 0.07	2.77 ± 0.06	2.82 ± 0.08
$\langle(\epsilon')^3\rangle$	14.1 ± 0.6	21.5 ± 1.6	19.9 ± 1.4	20.7 ± 2.1
$\langle(\epsilon')^4\rangle$	153 ± 14	388 ± 58	341 ± 48	364 ± 81
$\langle\epsilon^4\rangle/\langle\epsilon^2\rangle^2$	23.9	47.8	44.5	45.8
$\langle(\Omega')^2\rangle$	4.52 ± 0.09	5.19 ± 0.18	5.07 ± 0.19	5.20 ± 0.23
$\langle(\Omega')^3\rangle$	63.0 ± 3.1	100.0 ± 9.3	94.2 ± 9.9	97.6 ± 13.1
$\langle(\Omega')^4\rangle$	2022 ± 179	5315 ± 989	4920 ± 965	4751 ± 1200
$\langle\Omega^4\rangle/\langle\Omega^2\rangle^2$	99.2	197.1	191.3	175.9
		$R_\lambda\approx240$		
$k_{\max}\eta$	1.42	2.84	5.35	
$\langle(\epsilon')^2\rangle$	3.07 ± 0.05	3.17 ± 0.07	3.15 ± 0.06	
$\langle(\epsilon')^3\rangle$	25.3 ± 1.3	29.1 ± 1.8	28.8 ± 1.7	
$\langle(\epsilon')^4\rangle$	488 ± 53	696 ± 83	697 ± 89	
$\langle\epsilon^4\rangle/\langle\epsilon^2\rangle^2$	51.9	69.3	70.4	
$\langle(\Omega')^2\rangle$	5.81 ± 0.13	5.99 ± 0.18	5.93 ± 0.12	
$\langle(\Omega')^3\rangle$	133 ± 8	150 ± 14	142 ± 9	
$\langle(\Omega')^4\rangle$	8364 ± 1017	11222 ± 1869	10211 ± 1503	
$\langle\Omega^4\rangle/\langle\Omega^2\rangle^2$	247.7	312.8	290.6	

A further issue relevant to resolution effects on dissipation and enstrophy statistics is the behavior of ratios between their respective normalized moments $\langle(\Omega')^p\rangle/\langle(\epsilon')^p\rangle$. Such data for orders $p=2$, 3, and 4 are shown in Table III and seen to be less sensitive to resolution than moments of ϵ' and Ω' separately considered (as in Table II earlier). Likewise, resolution effects on the ratio

$$\frac{\langle\Omega^4\rangle/\langle\Omega^2\rangle^2}{\langle\epsilon^4\rangle/\langle\epsilon^2\rangle^2}$$

are weaker than on each quantity separately taken. The value of 4.8 for this ratio from our least-resolved simulation at $R_\lambda\approx240$ in Table III is not far from 5.26 reported by Chen *et al.*[6] in simulations at $R_\lambda=216$ with $k_{\max}\eta<2$ on a 512^3 grid.

Since results of the type shown in Table III are less sensitive to resolution, we have included data in this table from our two high-Reynolds-number simulations despite the modest degree of resolution in both. At $R_\lambda\approx390$, we see some difference between results at $k_{\max}\eta\approx1.37$ and 2.77 which, as will be seen later on, is related to the change of shape of the PDF of dissipation.

B. Error estimates

Analytic behavior in the limit of small r means that the longitudinal and transverse structure functions behave, respectively, as

$$\langle(\Delta_r u)^p\rangle/r^p=\langle(\partial u/\partial x)^p\rangle,\quad \langle(\Delta_r v)^p\rangle/r^p=\langle(\partial v/\partial x)^p\rangle. \tag{8}$$

In practice, since exact equality is not possible because of finite resolution, it is important to estimate deviations due to finite resolution, for each order p and a chosen value of r (i.e., the grid spacing Δx).

A Taylor expansion of $(\Delta_r v)/r$ for small r is

$$\frac{\Delta_r v}{r}=v_x+\frac{r}{2}v_{xx}+\frac{r^2}{6}v_{xxx}+O(r^3), \tag{9}$$

where, for brevity, coordinate subscripts are used to denote differentiation. Taking the pth power and assembling terms in ascending powers of r gives

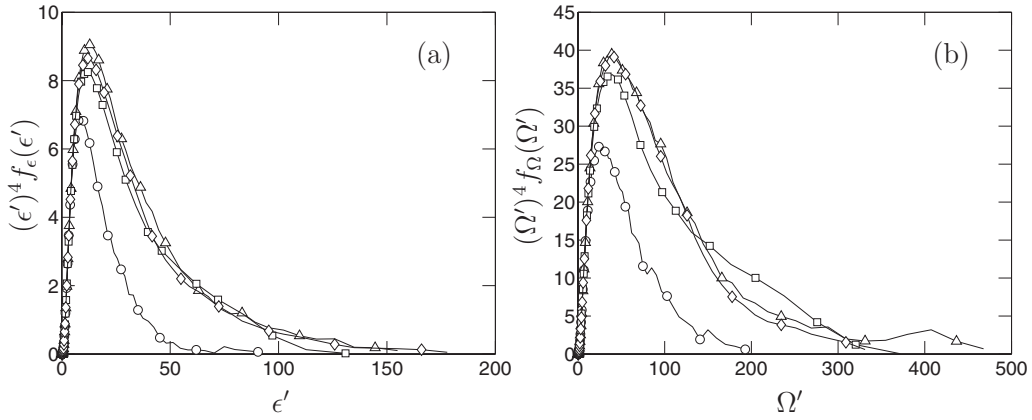

FIG. 5. Convergence test of contributions to fourth-order moments via integrands of PDFs of (a) normalized dissipation $\epsilon' \equiv \epsilon/\langle\epsilon\rangle$ and $\Omega' \equiv \Omega/\langle\Omega\rangle$, from several simulations at $R_\lambda \approx 140$ with different resolutions: $k_{\max}\eta \approx 1.41$ (○), 2.82 (△), 5.72 (□), and 11.2 (◇), corresponding to $\Delta x/\eta \approx 2$, 1, 1/2, and 1/4, respectively.

$$\left(\frac{\Delta_r v}{r}\right)^p - v_x^p = r\frac{p}{2}v_x^{p-1}v_{xx} + r^2 p \times\left(\frac{1}{6}v_x^{p-1}v_{xxx} + \frac{p-1}{8}v_x^{p-2}v_{xx}^2\right) + O(r^3). \tag{10}$$

We note the identities

$$v_x^{p-1}v_{xx} = \frac{1}{p}(v_x^p)_x \tag{11}$$

and

$$v_x^{p-1}v_{xxx} = (v_x^{p-1}v_{xx})_x - (p-1)v_x^{p-2}v_{xx}^2 \tag{12}$$

which imply that some of the contributions on the right of Eq. (10) vanish by homogeneity when averaged in space. We then obtain

$$\left\langle\left(\frac{\Delta_r v}{r}\right)^p\right\rangle - \langle v_x^p\rangle = -\frac{1}{24}p(p-1)r^2\langle v_x^{p-2}v_{xx}^2\rangle + O(r^4). \tag{13}$$

Because $\langle v_x^{p-2}v_{xx}^2\rangle$ is positive for all even integers p, this result is consistent with the observation that finite resolution underestimates high-order even moments. We also see that, to leading order, the error involved decreases as r^2 for structure functions of all orders p, but increases with p through the factor $p(p-1)$ as well as the quantity $\langle v_x^{p-2}v_{xx}^2\rangle$.

Equation (13) can be rewritten as

$$\frac{\langle v_x^p\rangle - \langle(\Delta_r v/r)^p\rangle}{\langle v_x^p\rangle} = \frac{p(p-1)}{24}Q_p^T\left(\frac{r}{\eta}\right)^2 + O(r^4), \tag{14}$$

where the effects of small-scale intermittency appear through the dimensionless quantity

$$Q_p^T \equiv \frac{\langle v_x^{p-2}v_{xx}^2\rangle}{\langle v_x^p\rangle/\eta^2}. \tag{15}$$

The analogous quantity Q_p^L can also be defined for longitudinal velocity gradients. The numerator of Q_p^T (and Q_p^L) is subject to Cauchy–Schwarz inequality for the covariance between two random variables (v_x^{p-2} and v_{xx}^2), whereas the denominator $\langle v_x^p\rangle$ can be modeled using lognormal or multifractal concepts. These quantities are readily extracted from our DNS database, although since second derivatives and higher powers of first derivatives are involved, we use only the best-resolved simulation at each Reynolds number.

Figure 6 shows DNS data on both Q_p^L and Q_p^T at $R_\lambda \approx 140$ ($k_{\max}\eta \approx 11.2$, $\Delta x/\eta \approx 1/4$). Since transverse gradients are statistically symmetric, we present only even-order results for Q_p^T. Although there is some scatter, there appears to be no clear dependence for $p > 4$ or so. An average from $p=4$ through 12 for both Q_p^L and Q_p^T is of the order of 0.05, with a weak increase at higher Reynolds numbers (not shown). Conclusions on the numerical value just cited and the weak dependence on the Reynolds number are both tentative, for stronger statements would require a closer study of resolution effects on second-order derivatives. In any case,

TABLE III. Ratios of moments of dissipation and enstrophy. The numbers here may slightly differ from those obtained using data in Table II since ensemble averaging is performed after taking the ratios for each realization.

R_λ	140	140	140	140	240	240	240	390	390	650
$k_{\max}\eta$	1.41	2.82	5.72	11.15	1.42	2.84	5.35	1.37	2.77	1.39
$\langle(\Omega')^2\rangle/\langle(\epsilon')^2\rangle$	1.8	1.8	1.8	1.8	1.9	1.9	1.9	2.0	2.0	2.0
$\langle(\Omega')^3\rangle/\langle(\epsilon')^3\rangle$	4.5	4.6	4.7	4.6	5.2	5.1	4.9	4.1	4.7	3.5
$\langle(\Omega')^4\rangle/\langle(\epsilon')^4\rangle$	13.3	13.8	14.1	12.7	17.2	15.7	14.5	4.7	9.2	4.5
$(\langle\Omega^4\rangle/\langle\Omega^2\rangle^2)/(\langle\epsilon^4\rangle/\langle\epsilon^2\rangle^2)$	4.2	4.2	4.2	3.7	4.8	4.4	4.1	1.2	2.4	1.2

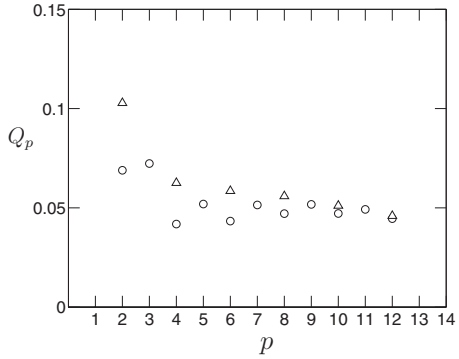

FIG. 6. Variation of Q_p^T (triangles) defined by Eq. (15) and its longitudinal counterpart (Q_p^L, circles) with order p, from the same highly resolved $R_\lambda \approx 140$ simulation, as in Figs. 1–3.

the main observation of near constancy for Q_p^L and Q_p^T at sufficiently large p is also supported by a simple scaling argument for the second derivative, i.e.,

$$v_{xx} \sim c\frac{v_x}{\eta}, \tag{16}$$

where (following Ref. 36) c may be taken to be a random coefficient of order unity. This estimate is consistent with the so-called p-model of intermittency[37] and leads to the result

$$Q_p^T = \frac{\langle v_x^{p-2} v_{xx}^2 \rangle}{\langle v_x^p \rangle / \eta^2} \approx \frac{\langle c^2 \rangle \langle v_x^{p-2} v_x^2 \rangle / \eta^2}{\langle v_x^p \rangle / \eta^2} = \langle c^2 \rangle, \tag{17}$$

which is independent of p but can retain a dependence on the Reynolds number.

The near constancy of Q_p^T suggests a $p(p-1)$ scaling for the normalized error in Eq. (14). This can be checked by computing the left hand side of Eq. (14) from the best-resolved simulation available at a given Reynolds number and comparing to the leading term $O(r^2)$ on the right hand side using the quasiconstant value of Q_p^T averaged over the range $p=4-12$. Figure 7 shows such a comparison at two Reynolds numbers $R_\lambda \approx 140$ and 240, with the estimated error evaluated for values of r corresponding to $k_{\max}\eta \approx 1.4$,

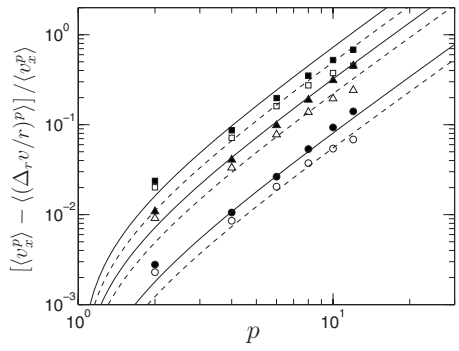

FIG. 7. Normalized departures from analytic behavior of transverse structure functions computed from DNS data, at $R_\lambda \approx 140$ with $k_{\max}\eta \approx 11.2$ (open symbols) and $R_\lambda \approx 240$ with $k_{\max}\eta \approx 5.35$ (closed symbols), compared to estimates based on Eq. (14) with quasiconstant values of Q_p^T. Circles, triangles, and squares denote data points at $r/\eta \approx 0.5$, 1, and 1.6, respectively. The dashed lines represent result from Eq. (14) for $R_\lambda \approx 140$; the solid lines for $R_\lambda \approx 240$.

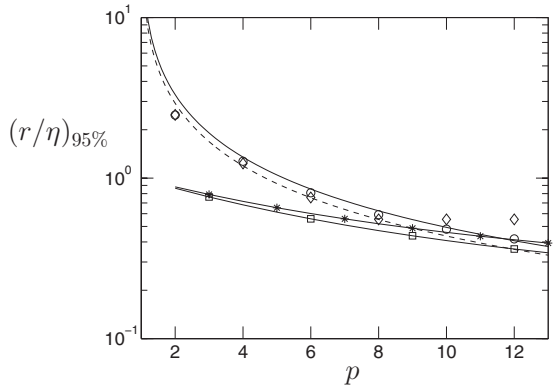

FIG. 8. Normalized scale size $(r/\eta)_{95}$ for 5% deviation from analytic behavior for different orders of moments of transverse velocity increments. DNS data from simulations at $R_\lambda \approx 140$ with $k_{\max}\eta \approx 11.2$ (circles) and 240 with $k_{\max}\eta \approx 5.35$ (diamonds) are compared to results from Eq. (18) at $R_\lambda \approx 140$ (solid line) and 240 (dashed line). Also included are the scales η_p/η [Eq. (6)] for $R_\lambda \approx 140$ (△) and 240 (□) as a continuous function of order p.

2.8, and 5.4 (see Table I). For all three levels of resolution very good agreement occurs between the actual (symbols) and estimated errors (lines) for orders up to 4, say. Agreement is less close for higher orders, which may be due to greater statistical uncertainty or a need to retain more terms in the Taylor series expansion in Eq. (9).

Using Eq. (14) and data of Fig. 6 on Q_p, it is possible to obtain a quantitative estimate of the value of r/η needed to capture structure functions of a chosen order p within a specified error tolerance. If the fractional error allowed at each order p is e, then Eq. (14) gives

$$(r/\eta)_{1-e} \approx \left[\frac{24e}{p(p-1)Q_p}\right]^{1/2} \tag{18}$$

as an estimate of the smallest scale size that must be resolved. As a working definition, we shall take $e=0.05$, i.e., accept a 5% error and denote the pertinent scale as $(r/\eta)_{95}$; however, other reasonably small choices of e will not have a material effect on the discussions below.

Figure 8 shows, at two Reynolds numbers, a comparison of $(r/\eta)_{95}$ computed from two different methods, as well as the theoretical estimate η_p/η [Eq. (6)] of Ref. 25. As expected from discussions of Figs. 6 and 7, results from errors directly based on the left hand side of Eq. (14) using the best-resolved simulations at each Reynolds number (circles and diamonds) are in close agreement with estimates based on Eq. (18) using quasiconstant values of Q_p^T from Fig. 6 (solid and dashed lines), except for the highest two orders ($p=10$ and 12) shown. It is clear that the smallest scale that must be resolved is a decreasing fraction of η as the moment-order increases; the conclusion on resolution applies, though less strongly, as the Reynolds number increases. These comparisons also suggest that, while the resolution requirements proposed by Yakhot and Sreenivasan may be overly restrictive for low orders, they become more accurate at higher orders.

A comment on the Reynolds number dependence of Eq. (18) from the perspective of Ref. 25 may be in order here. It may be noted that according to Eq. (6), η_2 (the scale needed

TABLE IV. Best-fit coefficients for Eqs. (20) and (21) in the range of $5<\epsilon',\Omega'<100$.

R_λ	$k_{\max}\eta$	b_Ω	b_ϵ	c_Ω	c_ϵ	b'_Ω	b'_ϵ	b'_Ω/b'_ϵ
140	1.41	5.23	6.04	0.29	0.33	7.11	10.54	0.67
140	2.82	7.04	8.27	0.24	0.25	6.42	8.51	0.75
140	5.72	6.46	9.54	0.25	0.23	6.54	8.51	0.77
140	11.15	7.25	8.79	0.23	0.25	6.44	8.57	0.75
240	1.42	6.96	6.75	0.23	0.28	6.14	8.41	0.73
240	2.84	7.40	8.55	0.22	0.24	6.07	7.92	0.77
240	5.35	6.78	8.62	0.24	0.24	6.12	7.91	0.77
390	1.37	8.29	8.96	0.20	0.22	5.59	7.20	0.78
390	2.80	8.89	10.74	0.19	0.19	5.47	6.76	0.81
650	1.39	8.96	8.63	0.18	0.22	5.32	6.65	0.80

to resolve second-order structure functions) is the same as η if $\zeta_2=2/3$ as in the K41 theory (and $\zeta_3=1$ exactly), but not if intermittency corrections for the second order are taken into account. Consistency with Ref. 25 then requires that η in Eq. (16) be replaced by η_2, which in turns leads to $Q_p^T\approx\langle c^2\rangle\times(\eta/\eta_2)^2$ in place of Eq. (17). Substitution of this relation into Eq. (18) then yields

$$(r/\eta)_{1-e}\approx\left[\frac{24e}{p(p-1)}\right]^{1/2}\langle c^2\rangle^{-1/2}\left(\frac{R_\lambda^{\ 2}}{15}\right)^{d_2+3/4}, \tag{19}$$

where $d_2=1/(\zeta_2-2)$ in terms of the inertial-range scaling exponent of the second-order structure function. In K41 phenomenology, with $d_2=-3/4$, the Reynolds number dependence in this expression vanishes. However, by using $\zeta_2=0.7$, which is now believed to be correct (see Ref. 25), the resulting weak Reynolds number dependence can be expressed as $R_\lambda^{-\gamma}$ with $\gamma=0.038$. Equation (19) can also be inverted to show that the relative error e scales as $\sim p(p-1)R_\lambda^{\ 2\gamma}$. Computations from the data appear to be consistent with these conclusions even though highly resolved simulations ($k_{\max}\eta>3$) are at present available only at $R_\lambda\approx140$ and 240, for which a wide inertial range is not yet attained.

III. REYNOLDS NUMBER SCALING

A. PDFs of dissipation and enstrophy

Past studies[38–40] have suggested that the dissipation PDF f_ϵ can be fitted well by a stretched exponential of the form

$$f_\epsilon(\epsilon')\sim\exp[-b_\epsilon(\epsilon')^{c_\epsilon}]. \tag{20}$$

A similar form for the enstrophy PDF, f_Ω, has also been proposed,[41] with prefactor and exponent denoted by b_Ω and c_Ω, respectively. Our interest here concerns the systematic effects of Reynolds number and grid resolution on the prefactors and the exponents.

Table IV gives the values of parameters which provide the best fits for the DNS data on the PDF normalized dissipation and enstrophy (ϵ' and Ω') in the range of 5–100, which captures the stretched-exponential behavior up to the largest fluctuations usually reported in experiments. The effects of Reynolds number and grid resolution are mainly evident in the exponents c_ϵ and c_Ω, which have a stronger role than the algebraic prefactors b_ϵ and b_Ω in Eq. (20). Consistent with other results in the figures discussed in Sec. II, the resolution effect for data at $R_\lambda\approx140$ is especially pronounced between $k_{\max}\eta\approx1.4$ and 2.8. On the other hand, for $R_\lambda\approx240$, resolution effects are shifted toward the tails and less significant in parameters applicable to the range of $5\leqslant\epsilon',\ \Omega'\leqslant100$.

Table IV shows that, at both $R_\lambda\approx140$ and 240, the exponents converge to about 0.25, in contrast with the past findings[8,40,42] which supported an exponent of about 1/2. In Fig. 9 we show the PDFs of dissipation and enstrophy from our datasets at $R_\lambda\approx140$ and 240 and the highest resolutions available ($k_{\max}\eta\approx11.2$ and 5.4, respectively). Very good agreement is seen with fits of the form (dashed lines)

$$f_\epsilon(\epsilon')\sim\exp[-b'_\epsilon(\epsilon')^{1/4}], \tag{21}$$

where the Reynolds number dependence is now expressed solely through the alternative algebraic prefactor b'_ϵ. The closeness of fit in this figure is virtually the same as that obtained using Eq. (20) and Table IV, at least for fluctuations

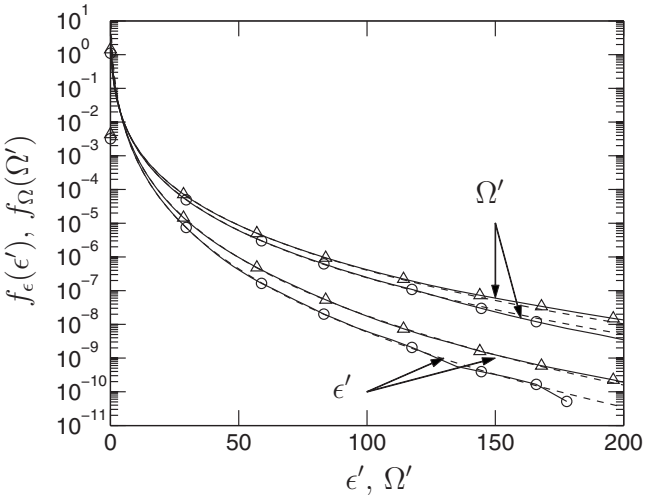

FIG. 9. PDFs of dissipation and enstrophy, at $R_\lambda\approx140$ with $k_{\max}\eta\approx11.2$ (○) and $R_\lambda\approx240$ with $k_{\max}\eta\approx5.35$ (△). The dashed lines represent stretched-exponential fits in the form of Eq. (21), which provides almost perfect agreement with the DNS data.

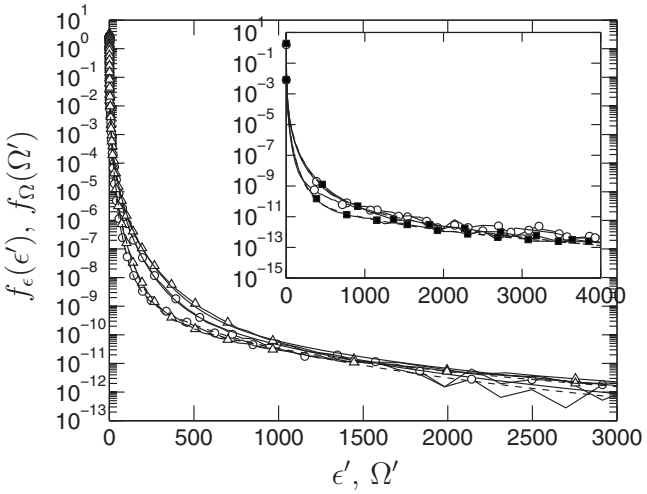

FIG. 10. PDF of dissipation (lower curves) and enstrophy (upper curves) from simulations at the highest two Reynolds numbers: $R_\lambda \approx 390$ at 1024^3 (○) and $R_\lambda \approx 650$ at 2048^3 (△), both with $k_{\max}\eta$ in the of range of 1.3–1.4. The dashed and unmarked solid lines (partly hidden) represent fits according to Eq. (22) for dissipation and enstrophy, respectively. The inset shows data from a more highly resolved simulation at $R_\lambda \approx 390$, with $k_{\max}\eta \approx 2.77$ (■) in comparison to $k_{\max}\eta \approx 1.4$ (○).

of moderately large magnitude which are typical of most laboratory measurements reported in the past. Both b'_ϵ and b'_Ω decrease with increasing Reynolds number, as shown on the right in Table IV. There is also an asymptotic decrease with increasing grid resolution at $R_\lambda \approx 140$, although, as suggested in the paragraph above, the corresponding resolution effects at $R_\lambda \approx 240$ may be obscured by the choice of the fitting range. In addition, we note that the ratio between b'_ϵ and b'_Ω is much less sensitive to Reynolds number than b'_ϵ and b'_Ω separately. This suggests that the trend for f_ϵ and f_Ω to approach each other at increasing Reynolds number is very slow.

The higher the Reynolds numbers, the wider the tails of f_ϵ and f_Ω; for these tails, there is no *a priori* reason for the functional forms suitable for the range of $5 \leqslant \epsilon', \Omega' \leqslant 100$ to continue to apply. In Fig. 10 we compare the PDFs at $R_\lambda \approx 390$ and 650. Despite the fact that our simulations are not highly resolved ($k_{\max}\eta$ between 1.4 and 2.8), it is clear that the PDF tails are very wide, extending to several thousand times the mean. This is a regime of extreme events which, except perhaps in reacting flows,[43] has not been reported in detail in the literature before. However, the existence of such extreme fluctuations is expected on theoretical grounds. Nelkin,[44] for instance, examined the scaling of extreme events in terms of local averages of energy dissipation rate ϵ_r and the ratio

$$\epsilon_r^{(\infty)} \equiv \lim_{n\to\infty} \frac{\langle \epsilon_r^{n+1} \rangle}{\langle \epsilon_r^n \rangle}.$$

Whereas an essential feature is that $\epsilon_r^{(\infty)}$ may scale as $r^{-2/3}$ according to Ref. 45, a scaling of the form r^{-1} was also suggested as a possibility. These two possible scaling relations imply that, at the smallest scale given by Eq. (7), one has $\epsilon_{\eta_{\min}}^{(\infty)} \sim R_\lambda^{4/3}$ and $\sim R_\lambda^2$, respectively. Although it is not possible to directly obtain $\epsilon_r^{(\infty)}$ from simulations, one could take the ∞-norm (i.e., the maximum value observed) as a measure of the most intense events. For example, the maximum values of ϵ' and Ω' from $R_\lambda \approx 240$ simulations at $k_{\max}\eta \approx 6$ are $O(500)$ and $O(700)$. Extrapolation using even the weaker estimate $\epsilon_{\eta_{\min}}^{(\infty)} \sim R_\lambda^{4/3}$ would suggest the occurrence of fluctuations of $O(1800)$ and $O(2600)$ at $R_\lambda \approx 650$. Although these simple calculations are only a rough estimate due to the statistical difficulty in obtaining the ∞-norm of any quantity, they are consistent with fluctuations in the range observed in our simulations (as in Fig. 10).

Unlike the situation at moderate Reynolds numbers, the extreme tails discussed above are not well described by fits of the forms of Eqs. (20) and (21). However, we find a uniformly good fit for essentially all values of ϵ' in the form of a double stretched exponential,

$$f_\epsilon(\epsilon') \sim s_1 \exp[-t_1(\epsilon')^{1/4}] + s_2 \exp[-t_2(\epsilon')^{1/4}] \qquad (22)$$

[and similarly for $f_\Omega(\Omega')$]. The best-fit coefficients corresponding to the dashed lines in Fig. 10 are shown in Table V. It is apparent from the contrast between the magnitudes of these parameters that the second exponential is significant primarily at the far tails. However, the most remarkable feature is that the PDFs of ϵ and Ω appear to virtually coincide in the limit of extreme ϵ' and Ω' (of order of 1000 or greater). The feature is observed in our data at both $R_\lambda \approx 390$ and 650 but not at lower Reynolds numbers, even in those simulations with very good resolution. This observation suggests the possibility of identical scaling of extreme events—which in turn can lead to similar scaling of high-order moments of energy dissipation and enstrophy, while differences could remain at lower orders for finite Reynolds numbers.

TABLE V. Best-fit coefficients for Eq. (22) for data at $R_\lambda \approx 390$ ($5 \leqslant \epsilon', \Omega' \leqslant 2000$) and 650 ($5 \leqslant \epsilon', \Omega' \leqslant 3000$).

R_λ	$k_{\max}\eta$	Variable	s_1	t_1	s_2	t_2
390	1.37	ϵ'	27.9	5.41	9.38×10^{-6}	2.19
390	1.37	Ω'	429.6	7.17	6.95×10^{-6}	2.19
390	2.77	ϵ'	13.1	5.10	10.4×10^{-6}	2.28
390	2.77	Ω'	81.7	6.37	0.17×10^{-6}	1.78
650	1.39	ϵ'	12.9	4.99	2.70×10^{-6}	1.93
650	1.39	Ω'	131.7	6.44	0.54×10^{-6}	1.73

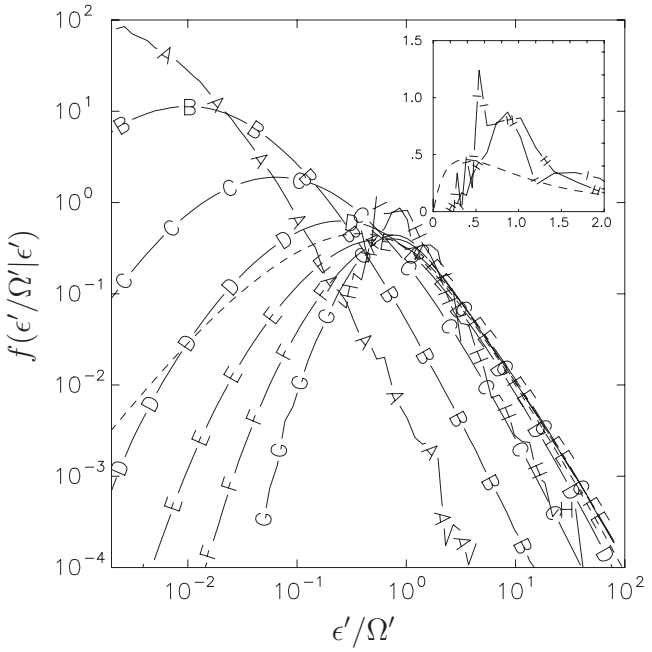

FIG. 11. Conditional PDF of the ratio ϵ'/Ω' given ϵ' in the $R_\lambda \approx 650$ simulation. Lines A-I correspond to $\epsilon' = 2^n$ with $n = -12, -9, -6, -3, 0, 3, 6, 9$, and 12 (note that lines H and I are seen more clearly in the inset, plotted in different scales). The dashed lines correspond to the unconditional PDF.

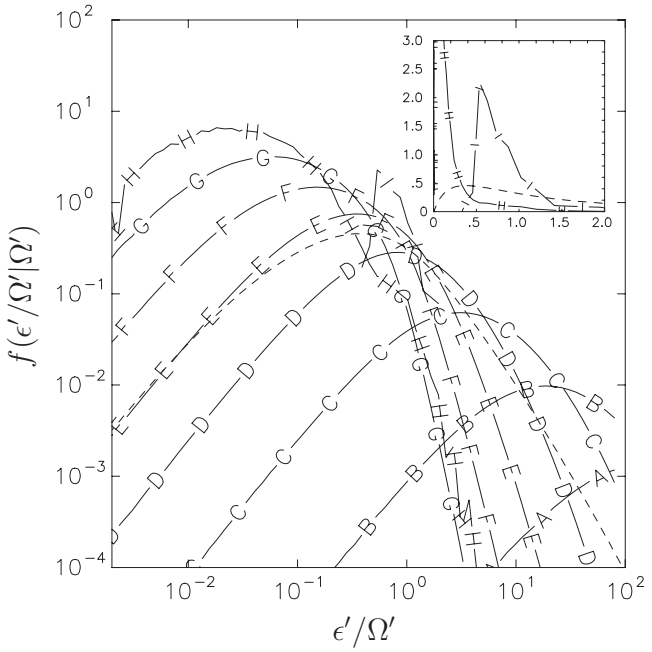

FIG. 12. Same as Fig. 11, but conditioned on Ω'.

As a check for possible resolution effects, we have included in Fig. 10 an inset which shows a direct comparison between simulations at $R_\lambda \approx 390$ using 1024^3 and 2048^3 grid points. The qualitative behaviors observed at these two resolutions are evidently very similar at the extreme tails of their PDFs, which virtually coincide. There is a difference at intermediate values of dissipation, where the dissipation PDF obtained from the lesser-resolved simulation lies appreciably above the PDF from the better-resolved simulation. While this difference may be in part statistical, it is also consistent with the expectation that lesser resolution would lead to local smoothing of some of the most intense velocity gradient fluctuations, with the possible consequence that the number of samples of moderately large (instead of extremely large) dissipation would be increased. We also note that normalized ratios at this Reynolds number in the last two rows of Table III appear to follow a trend of resolution effects different from those at $R_\lambda \approx 140$ and 240. However, we have examined the spread in numbers among all the realizations processed and have found also substantial variability in these results.

As an aside, we note that although the present DNS data, as well as past studies, are consistent with Eq. (21) in providing a good fit for low R_λ [or Eq. (22) for higher R_λ], these fits are different from the functional forms derived either from the Yakhot's theory[46] or multifractal concepts.[47] We cannot, of course, be entirely certain as to how an even finer resolution might change the picture.

Since two random variables with the same PDFs can be unrelated to each other, we now ask whether the extreme values of ϵ' and Ω' of the order 10^3 discussed above indeed occur in spatial proximity to each other. We note that the single-point correlation between dissipation and enstrophy is positive and increases with the Reynolds number (see, e.g., Refs. 48 and 49; or Refs. 50 and 51, for data inferred from Lagrangian cross-correlation functions). Since correlation coefficients are second-order quantities, they are not much affected by resolution: e.g., in our present data at $R_\lambda \approx 140$ the dissipation-enstrophy correlation varies only between 0.50 and 0.51 for $k_{\max}\eta \approx 1.41-11.15$. The increase with Reynolds number is also relatively mild, from 0.51 at $R_\lambda \approx 140$ to 0.56 at $R_\lambda \approx 650$. These observations may suggest only a modestly increased coincidence of extreme events in dissipation and enstrophy. This tendency can be quantified by considering conditional statistics: in particular, if extreme ϵ' and Ω' are collocated in space, the PDF of the ratio ϵ'/Ω' given large ϵ' or large Ω' should show a peak close to unity in the sample space.

In Fig. 11, we show data at $R_\lambda \approx 650$ on the conditional PDF of ϵ'/Ω', given a range of values of ϵ' chosen in geometric progression. In general, as the conditioning value of ϵ' increases, larger values of ϵ'/Ω' become more likely, and the conditional PDF shifts to the right. However, as ϵ' increases beyond the mean, the right tail of the PDF ceases to increase (lines D to G) and eventually drops back (lines H and I). Furthermore, for very large ϵ' (lines H and I, in inset) the conditional PDF is seen to form a peak in the neighborhood of $\epsilon'/\Omega' \approx 1$. These observations indicate that the moderately large dissipation is not usually accompanied by small enstrophy (which would make the ratio ϵ'/Ω' large), while very large values of dissipation are likely to be accompanied by similarly large enstrophy (which makes the ratio ϵ'/Ω' close to 1).

The converse of the result above is examined in Fig. 12, which shows the effects of conditioning on Ω'. As expected, the ratio ϵ'/Ω' tends to be smaller as the conditioning enstrophy increases, and the PDF shifts to the left (as shown in lines A to G). For conditioning enstrophy that is equal to the

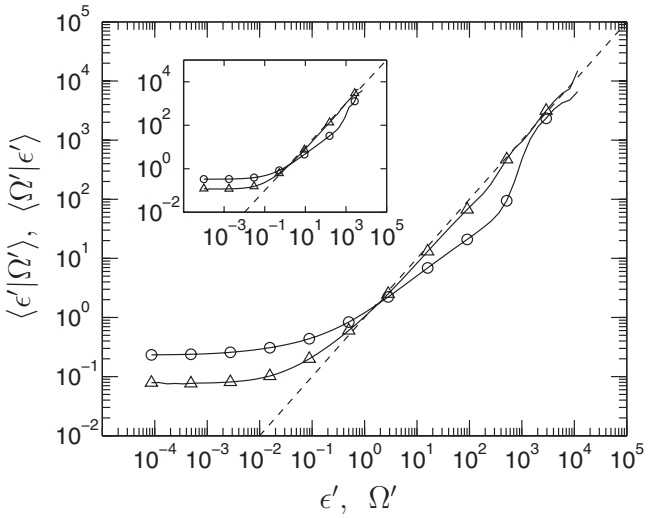

FIG. 13. Conditional means $\langle \epsilon' | \Omega' \rangle$ (○) and $\langle \Omega' | \epsilon' \rangle$ (△) at $R_\lambda \approx 650$ with $k_{\max}\eta \approx 1.41$. A dashed line at slope of 1.0 is included for comparison. The inset shows results at $R_\lambda \approx 390$ with $k_{\max}\eta \approx 2.77$.

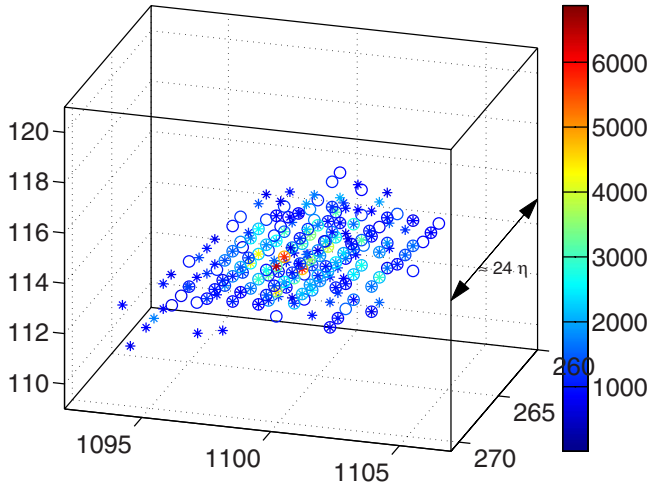

FIG. 14. (Color online) Sample of cluster of grid points with $\epsilon' > 800$ (circles) and $\Omega' > 800$ (crosses) at $R_\lambda \approx 650$ with $k_{\max}\eta \approx 1.4$. Colors indicate intensity of ϵ' and Ω'.

unconditional mean (line E), the likelihood for $\epsilon'/\Omega' < 1$ is very close to that in unconditional data (dashed curve). This implies that in regions of average enstrophy, there is no tendency for stronger-than-average dissipation to develop. However, a different trend (lines H and I, in inset) is seen at very large enstrophy values, with the PDF shifting back to the right and small values of ϵ'/Ω' eventually becoming less likely. For the most intense enstrophy (line I, $\Omega' \approx 4 \times 10^3$) most samples for ϵ/Ω' are apparently between 0.5 and 1. This indicates that events of most intense enstrophy are often accompanied by fairly large but less intense dissipation. Alternatively, we can infer that the mechanisms causing extreme enstrophy either contribute less to dissipation or are subject to some partial cancellation by competing effects.

Additional information on the duality above can be obtained from the conditional averages of either ϵ and Ω given the other, as shown in Fig. 13. For low ϵ or low Ω, the conditional dependencies are relatively weak: i.e., there is no strong correlation between dissipation and enstrophy in regions of relative quiescence. A dashed line of slope 1 is drawn to indicate the limiting condition of large ϵ and Ω being coincident. For $\epsilon > \langle \epsilon \rangle$ the behavior of $\langle \Omega | \epsilon \rangle$ is close to this limit: i.e., large dissipation is most likely accompanied by large enstrophy, as inferred above from conditional PDFs in Fig. 11. On the other hand, $\langle \epsilon | \Omega \rangle$ falls below the line of slope unity for Ω' between 10 and 1000, which indicates that enstrophy values in this range are quite often accompanied by smaller dissipation. However, $\langle \epsilon | \Omega \rangle$ appears to return toward the line of slope of 1 (though slightly on the low side) when Ω' exceeds 1000, indicating that the extreme events of high enstrophy may be accompanied by extreme dissipation as well. These trends are also consistent with the unconditional PDFs shown in Fig. 10: i.e., dissipation and enstrophy scale differently for ϵ' and Ω' roughly in the range of 10–1000, but similarly for extreme fluctuations exceeding about 1000 times the mean. Similar trends are also evident in the inset of Fig. 13 which shows data at the lower R_λ of 390 but higher resolution. Resolution effects are generally much weaker in statistics conditioned upon a highly intermittent variable such as dissipation or enstrophy fluctuations, as reported in Ref. 10 (see also later in Sec III B).

Although the filamentlike nature of intense vortical structures is well known,[52,53] the connection between regions of high dissipation and enstrophy in their topologies and spatial distribution is difficult to quantify. A recent study by Moisy and Jiménez[54] shows results for moderate fluctuations consistent with ours, in that the enstrophy is found to be more intermittent and that high activity regions appear in clusters rather than as random distributions in space. However, their Reynolds numbers were lower than ours and presumably not sufficiently high to observe the collapse between the tails of dissipation and enstrophy PDFs suggested in our Fig. 10. For the present data, while single-point statistics indicate that large dissipation and enstrophy do not coincide except for extreme values, a significant overlap in space is still possible. A simple but direct test of such a possibility is to examine the coordinate locations of either ϵ' or Ω' exceeding a chosen threshold h. Figure 14 shows a typical cluster of points above a normalized threshold $h = 800$ (which incidentally is much higher than those used by other researchers to define "intense" events), in an instantaneous velocity field taken from the 2048^3 simulation ($R_\lambda = 650$). Points of high ϵ' and high Ω' are indicated by asterisks and open circles, respectively, and a color map is used to illustrate the intensity. A substantial overlap is indicated by the presence of asterisks placed in a circle, especially in the core of the cluster shown.

Despite the qualitative nature of Fig. 14, it is clear that the size of the clusters shown here decreases with increasing threshold. We can estimate the average size of the cluster by identifying a subdomain that just completely encloses the cluster (as in Fig. 14). A volume V_h can be defined by multiplying the number of samples with $\epsilon' > h$ within the subdomain by the volume of a grid cell [which is $(\Delta x)^3$]. Without making specific assumptions on the topology of each cluster, a rough measure of linear size can be obtained as

$\Lambda_\epsilon(h)=V_h^{1/3}$, and similarly as $\Lambda_\Omega(h)$ for regions of high enstrophy. Our results suggest power-law dependencies of the forms $\Lambda_\epsilon(h)\sim h^{-0.54}$ and $\Lambda_\Omega(h)\sim h^{-0.68}$ for threshold levels in the extreme range. While these relations involve proportionality factors which increase with the Reynolds number, the exponents deduced from simulations at $R_\lambda\approx 390$ and 650 are nearly the same, suggesting a robust degree of asymptotic behavior. Similar results are obtained also for an alternative (and larger) estimate of linear size as the maximum distance between any two points with $\epsilon'>h$ or $\Omega>h$ within the same cluster, with the best-fit exponents being about −0.8 and −0.9, respectively.

A final note on resolution effects and the detection of flow structures is appropriate here. Regions of high ϵ or Ω are likely to have at least one linear dimension significantly shorter than the estimates considered above. For example, Λ_ϵ/η and Λ_Ω/η lie typically in the range of 10–50 for $h=1000$ in simulations $R_\lambda\approx 650$—and so can be detected easily—while the shortest linear dimension is much smaller and harder to resolve. In other words, a simulation with the "standard" grid resolution $k_{\max}\eta\approx 1.5$ ($\Delta x\approx 2\eta$) can capture only some of the characteristics of high intensity clusters.

B. Conditional sampling of velocity gradient contributions

Since fluctuations in both dissipation and enstrophy are the result of velocity gradient fluctuations in the flow, it is useful to examine the properties of different groupings of velocity gradient fluctuations associated with high intensity events. In shorthand, we may write

$$\epsilon/\nu = L + T + C, \quad \Omega = T - C, \tag{23}$$

where, without using the standard summation convention,

$$L = 2\sum_{i=1,3} u_{i,i}^2, \quad T = \sum_{i,j=1,3}^{i\neq j} u_{i,j}^2, \quad \text{and } C = \sum_{i,j=1,3}^{i\neq j} u_{i,j}u_{j,i}. \tag{24}$$

Longitudinal gradients contribute to term L only, and both longitudinal and transverse terms (L and T) are always positive, whereas the cross-term C may be of either sign depending on how the off-diagonal velocity gradient components are correlated with each other. A positive C tends to contribute to higher dissipation, whereas a negative C may lead to higher enstrophy. We use conditional sampling below to characterize the relative roles of the terms L, T, and C in regions of high dissipation or enstrophy, in comparison to unconditional statistics averaged over the entire flow domain.

The standard local isotropy relation $\langle\epsilon\rangle=15\nu\langle u_{1,1}^2\rangle$ for incompressible homogeneous turbulence readily leads to the result

$$\langle L\rangle = (2/5)\langle\epsilon\rangle/\nu, \tag{25}$$

while the other two contributions can be written as

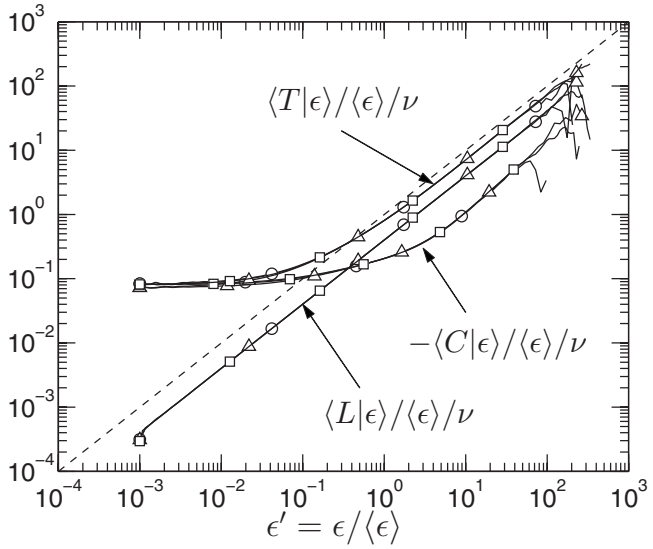

FIG. 15. Conditional averages $\langle L|\epsilon\rangle$, $\langle T|\epsilon\rangle$, and $-\langle C|\epsilon\rangle$, all normalized by $\langle\epsilon\rangle/\nu$, from simulations at $R_\lambda\approx 240$ and different degrees of resolution: $k_{\max}\eta\approx 1.42$ (○), 2.84 (△), and 5.35 (□). A dashed line of slope of 1.0 is included for comparison.

$$\langle T\rangle = 2\langle L\rangle, \quad \langle C\rangle = -\langle L\rangle/2. \tag{26}$$

One possible scenario for large dissipation and enstrophy to scale similarly is for these two relations to be generalized to conditional averages given large dissipation and enstrophy, e.g.,

$$\langle L|\epsilon\rangle = \frac{2}{5}\frac{\epsilon}{\nu}, \tag{27}$$

or at least show a trend toward this behavior in the limit of very large ϵ. A second possibility is for transverse gradients to dominate the largest fluctuations of ϵ and Ω overwhelmingly, such that

$$T \gg (L, |C|). \tag{28}$$

This is a conjecture motivated by the fact that transverse gradients are generally more non-Gaussian and have a greater tendency to exhibit larger fluctuations.[55,21] Conditional sampling is expected to reveal which of these two scenarios correctly represent the data.

Basic results including a resolution check on the averages of L, T, and $-C$ conditioned upon the local dissipation rate are given in Fig. 15, using data from simulations at $R_\lambda\approx 240$ with three different values of the resolution parameter $k_{\max}\eta$. Since $\langle C|\epsilon\rangle$ is found to be negative for all ϵ, we have plotted $\langle -C|\epsilon\rangle$ instead. Except for better capture of samples at large ϵ, the effect of grid resolution on these quantities is apparently weak (which is true for conditional statistics in other contexts as well, e.g. see Ref. 10). A dashed line of slope of 1 on logarithmic scales shows that the conditional average of longitudinal gradients behaves in almost the same way as the unconditional result of Eq. (25), i.e., Eq. (27). It is perhaps remarkable that this result holds literally for *all* values of ϵ; in the Appendix we provide some theoretical support for this result. A similar scaling is also evident for the other terms, $\langle T|\epsilon\rangle$ and $\langle C|\epsilon\rangle$ for $\epsilon'>4$. On the other hand, in

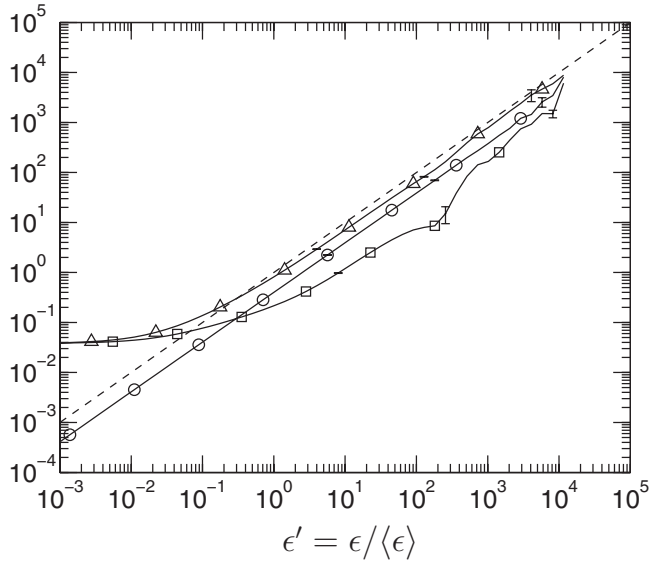

FIG. 16. Conditional averages $\langle L|\epsilon\rangle/\langle\epsilon\rangle/\nu$ (○), $\langle T|\epsilon\rangle/\langle\epsilon\rangle/\nu$ (△), and $-\langle C|\epsilon\rangle/\langle\epsilon\rangle/\nu$. (□) at $R_\lambda \approx 650$ with $k_{\max}\eta \approx 1.39$. The dashed line has slope of 1.0.

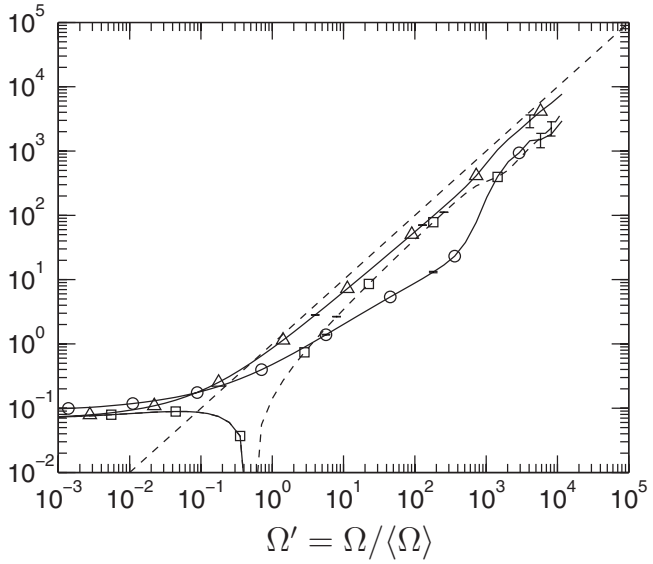

FIG. 17. Same as Fig. 16, but conditioned on normalized enstrophy instead of dissipation. Since the term $\langle C|\Omega'\rangle/\langle\Omega\rangle$ changes sign, solid and dashed lines are used to represent positive and negative values of it, respectively.

the limit of low ϵ, both $\langle T|\epsilon\rangle$ and $\langle C|\epsilon\rangle$ are of nearly the same magnitude but opposite signs. This effect can be understood by noting that the strain rates, both off-diagonal and diagonal, must become small as $\epsilon \to 0$. For example, $\epsilon \to 0$ implies $s_{12}^2 = (u_{1,2}^2 + u_{2,1}^2 + 2u_{1,2}u_{2,1}) \to 0$ which, upon summation of different components and conditional averaging, leads to $\langle C|\epsilon\rangle \approx -\langle T|\epsilon\rangle$.

Figure 16 shows corresponding data on conditional averages from our highest Reynolds number simulation ($R_\lambda \approx 650$). Although many features are broadly similar to those at lower Reynolds number (see the preceding figure), there are significant differences in the behavior of $\langle -C|\epsilon'\rangle$ in the range of $\epsilon' > 1000$ and in comparisons among L, T, and C for extremely large dissipation. To understand this property, we note that as ϵ' increases in level from small to moderate, and from moderate to extreme, the conditional distribution of C changes from having only negative samples to having a small number of positive samples, and finally to having a wide range of both positive and negative samples, with the conditional mean remaining negative. The "kink" seen in $\langle -C|\epsilon\rangle$ at ϵ' around 300 is the result of partial cancellation between positive and negative samples, which also leads to increased noise that persists to very large dissipation. However, despite this uncertainty, it can be seen that the ratio of $T:L:C$ becomes closer to the isotropic value of $2:1:-1/2$ from $\epsilon' \approx 10^3$ and upward. This suggests that, within the limits of sampling uncertainties, motions contributing to events of extreme dissipation are nearly isotropic in their statistical properties. Furthermore, as can be seen from Eq. (23), such a ratio also implies similar scaling for extreme dissipation and enstrophy.

To consider regions of high enstrophy, we show the results from high Reynolds number again in Fig. 17, this time conditioned on enstrophy instead of on dissipation. Since $\Omega \equiv T - C$, it is not surprising that $\langle C|\Omega\rangle$ is positive for low Ω (solid line with circles) and negative for high Ω (dashed line). For very low Ω, we observe $T \approx C$, which can again be explained by kinematics as $\Omega \to 0$, while L, which contributes only to ϵ, is nearly constant. In a narrow range of Ω' around unity the ratio between $\langle T|\Omega\rangle$ and $-\langle C|\Omega\rangle$ is close to 4, as suggested by Eq. (26). Larger values of Ω' up to about 400 are seen to be the result of C and $-T$ approaching each other as they increase in magnitude. Remarkably, however, as Ω' approaches about 1000, the ratio between $\langle T|\Omega\rangle$ and $-\langle C|\Omega\rangle$ becomes close to 4 again. In other words, these results suggest that the local flow structure is close to statistically isotropic in regions of extreme enstrophy, as already noted for extreme dissipation. This result is consistent with a trend toward identical scaling of extreme events in dissipation and enstrophy, which was suggested earlier in this paper via the PDFs in Fig. 10.

IV. DISCUSSION AND CONCLUSIONS

We have used data from DNS of isotropic turbulence with up to 2048^3 grid points to examine the scaling with increasing Reynolds number of dissipation and enstrophy fluctuations. To establish the veracity of results, we have studied the effects of numerical resolution on small-scale statistics, keeping in mind the recent resolution criteria[25] advocated for attaining accurate data. We have obtained data at different resolutions and Reynolds numbers and examined, in particular, if large fluctuations of dissipation and enstrophy tend to scale in the same way at high Reynolds number.

Results at Taylor-scale Reynolds number $R_\lambda \approx 140$ indicate that moments of dissipation and enstrophy are accurate up to fourth order if the product of the highest resolvable wavenumber ($k_{\max}$) and Kolmogorov length scale (η) is at least 3, or, equivalently, the grid spacing is equal to η or smaller. The constraint becomes stronger with increasing R_λ and increasing order of the moment. A Taylor-series expansion is used to quantify the degree of departure from the analytic range in structure functions of different orders and

as a function of the Reynolds number. This analysis leads to error estimates for finite resolution and finite Reynolds numbers. Although the use of the standard resolution of $k_{\max}\eta \approx 1.5$ leads to underestimation of high-order moment and the tails of PDFs of dissipation and enstrophy, statements comparing relative behaviors of these quantities appear to be qualitatively correct.

A common indicator of intermittency in dissipation and enstrophy is in the behavior of wide tails of their PDFs, which are well represented by stretched-exponential fits up to 100 times the mean. However, data at the two highest Reynolds numbers available ($R_\lambda \approx 390$ and 650) reveal extreme fluctuations as large as several thousands times the mean. We find that the tails of such PDFs can be described as sums of two (stretched) exponentials. This is a qualitative change of behavior from the low-Reynolds-number case. For extreme values of ϵ' and Ω', the PDFs appear to coincide within statistical error, suggesting a common behavior of extreme fluctuations even if low order statistics may still differ. These extreme fluctuations seem to approach a state of local isotropy. Results from conditional averaging indicate that regions of extreme dissipation and enstrophy possess a significant degree of overlap; but, while intense dissipation is often accompanied by intense enstrophy, intense enstrophy is less often accompanied by intense dissipation. The dimensions of clusters of points with dissipation or enstrophy above a certain threshold suggest that their presence can be readily detected even with $k_{\max}\eta \approx 1.5$, but some details will not be captured.

The nature of extreme fluctuations is studied further by decomposing both dissipation and enstrophy into longitudinal (L), transverse (T), and cross-term (C) contributions. In general, C is positive in strain-dominated regions, negative in rotation-dominated regions, and small compared to L and T whenever large dissipation and enstrophy occur simultaneously. The relative sizes of the terms L, T, and C associated with extreme events in dissipation and/or enstrophy appear to be consistent with a state of local isotropy. In the future it would be useful to re-examine the related issue of scalings of longitudinal versus transverse statistics (e.g., Refs. 55 and 56), accounting for resolution effects.

An important consideration for turbulence research as ever more powerful computer available is to recognize situations where more computer power needs to be directed at resolution effects in the numerical results. Extensions of this work are of interest for the passive scalar transport, where scalar gradient fluctuations contributing to the scalar dissipation are generally accepted as more intermittent and more demanding, depending on the Schmidt number, in terms of resolution requirements.

ACKNOWLEDGMENTS

This work has benefited substantially from discussions with Professor T. Gotoh, Professor J. Schumacher, and Professor V. Yakhot. We gratefully acknowledge financial support from the Fluid Dynamics Program of the National Science Foundation, via Grant Nos. CBET-0553867 (P.K.Y.) and CBET-0553602 (K.R.S.). Computations and data analyses were carried out using the resources of San Diego Supercomputer Center (SDSC), Pittsburgh Supercomputing Center (PSC), and the NERSC facility at the Lawrence Berkeley National Laboratory, U.S. Department of Energy.

APPENDIX: A LOCAL ISOTROPY RESULT FOR LONGITUDINAL VELOCITY GRADIENTS

We present a theoretical derivation for Eq. (27) which is supported by the observed behavior of the quantity $\langle L|\epsilon\rangle$ as in Figs. 15 and 16. The starting point is that local isotropy requires the fourth-order tensor $\langle u_{i,j}u_{k,l}\rangle$ to take the form (e.g., Pope[57])

$$\langle u_{i,j}u_{k,l}\rangle = \alpha\delta_{ij}\delta_{kl} + \beta\delta_{ik}\delta_{jl} + \gamma\delta_{il}\delta_{jk}, \tag{A1}$$

where the scalar coefficients α, β, and γ can, with the use of incompressibility, be expressed in terms of longitudinal and transverse velocity gradient variances $\langle(u_{1,1})^2\rangle$ and $\langle(u_{1,2})^2\rangle$. We propose that the same basic relation applies to conditional averages given a scalar variable which is itself statistically homogeneous in space. Accordingly, we write

$$\langle u_{i,j}u_{k,l}|\epsilon\rangle = \alpha(\epsilon)\delta_{ij}\delta_{kl} + \beta(\epsilon)\delta_{ik}\delta_{jl} + \gamma(\epsilon)\delta_{il}\delta_{jk}, \tag{A2}$$

but henceforth for simplicity, we will omit the functional dependence of α, β, and γ on ϵ in our notation. As for unconditional statistics incompressibility requires

$$3\alpha + \beta + \gamma = 0. \tag{A3}$$

For longitudinal gradients setting $i=j=1$ gives

$$\langle(u_{1,1})^2|\epsilon\rangle = \alpha + \beta + \gamma, \tag{A4}$$

whereas for transverse gradients setting $i=1$ and $j=2$ gives

$$\langle(u_{1,2})^2|\epsilon\rangle = \beta. \tag{A5}$$

By solving the above for α, β, and γ, and using the simple local isotropy results $\langle L|\epsilon\rangle = 6\langle(u_{1,1})^2|\epsilon\rangle$, $\langle T|\epsilon\rangle = 6\langle(u_{1,2})^2|\epsilon\rangle$ [where L, T, and C are defined as in Eq. (23)], we can rewrite Eq. (A2) as

$$\langle u_{i,j}u_{k,l}|\epsilon\rangle = -\frac{\langle L|\epsilon\rangle}{12}(\delta_{ij}\delta_{kl} - 3\delta_{il}\delta_{jk}) + \frac{\langle T|\epsilon\rangle}{6}(\delta_{ik}\delta_{jl} - \delta_{il}\delta_{jk}). \tag{A6}$$

For the cross terms, therefore, we have

$$\langle u_{1,2}u_{2,1}|\epsilon\rangle = \tfrac{1}{4}\langle L|\epsilon\rangle - \tfrac{1}{6}\langle T|\epsilon\rangle, \tag{A7}$$

and hence

$$\langle C|\epsilon\rangle = \tfrac{3}{2}\langle L|\epsilon\rangle - \langle T|\epsilon\rangle. \tag{A8}$$

Since by definition $\langle L|\epsilon\rangle + \langle T|\epsilon\rangle + \langle C|\epsilon\rangle = \epsilon/\nu$, substitution from Eq. (A8) now produces the result $\epsilon/\nu = (5/2)\langle L|\epsilon\rangle$ and hence Eq. (27) for the behavior of $\langle L|\epsilon\rangle$, which has been confirmed (Fig. 15) in our data to within sampling uncertainty.

It should be noted that an exact result as shown here is available only for $\langle L|\epsilon\rangle$ but not $\langle T|\epsilon\rangle$ or $\langle C|\epsilon\rangle$ separately (which would have to involve additional assumptions not well supported by the numerical data). Furthermore, whereas

conditioning by the enstrophy leads to a relation similar to Eq. (A8), since the contributions of T and C to Ω are different, no corresponding result applies for $\langle L|\Omega\rangle$.

[1] E. Siggia, "Numerical study of small-scale intermittency in three-dimensional turbulence," J. Fluid Mech. **107**, 375 (1981).
[2] R. M. Kerr, "Higher-order derivative correlations and the alignment of small-scale structures in isotropic numerical turbulence," J. Fluid Mech. **153**, 31 (1985).
[3] P. K. Yeung and S. B. Pope, "Lagrangian statistics from direct numerical simulations of isotropic turbulence," J. Fluid Mech. **207**, 531 (1989).
[4] A. Bershadskii, E. Kit, and A. Tsinober, "Strongly localized events of energy, dissipation, enstrophy and enstrophy generation in turbulent flows," Fluid Dyn. Res. **14**, 71 (1994).
[5] K. R. Sreenivasan, A. Juneja, and A. Suri, "Scaling properties of circulation in moderate-Reynolds-number turbulent wakes," Phys. Rev. Lett. **75**, 433 (1995).
[6] S. Chen, K. R. Sreenivasan, and M. Nelkin, "Inertial range scalings of dissipation and enstrophy in isotropic turbulence," Phys. Rev. Lett. **79**, 1253 (1997).
[7] T. Zhou and R. A. Antonia, "Reynolds number dependence of the small-scale structure in grid turbulence," J. Fluid Mech. **406**, 81 (2000).
[8] B. W. Zeff, D. D. Lanterman, R. McAllister, R. Roy, E. J. Kostelich, and P. Lathrop, "Measuring intense rotation and dissipation in turbulent flows," Nature (London) **421**, 146 (2003).
[9] P. K. Yeung, D. A. Donzis, and K. R. Sreenivasan, "High-Reynolds-number simulation of turbulent mixing," Phys. Fluids **17**, 081703 (2005).
[10] P. K. Yeung, S. B. Pope, A. G. Lamorgese, and D. A. Donzis, "Acceleration and dissipation statistics of numerically simulated isotropic turbulence," Phys. Fluids **18**, 065103 (2006).
[11] M. Nelkin, "Enstrophy and dissipation must have the same scaling exponents in the high Reynolds number limit of fluid turbulence," Phys. Fluids **11**, 2202 (1999).
[12] V. L'vov and I. Procaccia, "The universal scaling exponents of anisotropy in turbulence and their measurements," Phys. Fluids **8**, 2565 (1996).
[13] G. He, S. Chen, R. H. Kraichnan, R. Zhang, and Y. Zhou, "Statistics of dissipation and enstrophy induced by localized vortices," Phys. Rev. Lett. **81**, 4636 (1998).
[14] L. Chevillard and C. Meneveau, "Intermittency and universality in a Lagrangian model of velocity gradients in three-dimensional turbulence," C. R. Mec. **335**, 187 (2007).
[15] K. R. Sreenivasan and R. A. Antonia, "The phenomenology of small-scale turbulence," Annu. Rev. Fluid Mech. **29**, 435 (1997).
[16] M. S. Borgas and P. K. Yeung, "Relative dispersion in isotropic turbulence. Part 2. A new stochastic model with Reynolds-number dependence," J. Fluid Mech. **503**, 125 (2004).
[17] K. R. Sreenivasan, "An update on the dissipation rate in homogeneous turbulence," Phys. Fluids **10**, 528 (1998).
[18] D. A. Donzis, K. R. Sreenivasan, and P. K. Yeung, "Scalar dissipation rate and dissipative anomaly in isotropic turbulence," J. Fluid Mech. **532**, 216 (2005).
[19] V. Eswaran and S. B. Pope, "An examination of forcing in direct numerical simulations of turbulence," Comput. Fluids **16**, 257 (1988).
[20] L. P. Wang, S. Y. Chen, J. G. Brasseur, and J. C. Wyngaard, "Examination of hypotheses in the Kolmogorov refined turbulence theory through high-resolution simulations. Part 1. Velocity field," J. Fluid Mech. **309**, 113 (1996).
[21] T. Gotoh, D. Fukayama, and T. Nakano, "Velocity field statistics in homogeneous steady turbulence obtained using a high-resolution direct numerical simulation," Phys. Fluids **14**, 1065 (2002).
[22] Y. Kaneda, T. Ishihara, M. Yokokawa, K. Itakura, and A. Uno, "Energy dissipation rate and energy spectrum in high resolution direct numerical simulations of turbulence in a periodic box," Phys. Fluids **15**, L21 (2003).
[23] L. Biferale, G. Boffetta, A. Celani, B. J. Devenish, A. Lanotte, and F. Toschi, "Multifractal statistics of Lagrangian velocity and acceleration in turbulence," Phys. Rev. Lett. **93**, 064502 (2004).
[24] K. R. Sreenivasan, "Possible effects of small-scale intermittency in turbulent reacting flows," Flow, Turbul. Combust. **72**, 115 (2004).
[25] V. Yakhot and K. R. Sreenivasan, "Anomalous scaling of structure functions and dynamic constraints on turbulence simulations," J. Stat. Phys. **121**, 823 (2005).
[26] J. Schumacher, K. R. Sreenivasan, and P. K. Yeung, "Very fine structures in scalar mixing," J. Fluid Mech. **531**, 113 (2005).
[27] J. Schumacher, K. R. Sreenivasan, and V. Yakhot, "Asymptotic exponents from low-Reynolds-number flows," New J. Phys. **9**, 89 (2007).
[28] T. Watanabe and T. Gotoh, "Inertial-range intermittency and accuracy of direct numerical simulation for turbulence and passive scalar turbulence," J. Fluid Mech. **590**, 117 (2007).
[29] T. Ishihara, Y. Kaneda, M. Yokokawa, K. Itakura, and A. Uno, "Small-scale statistics in high-resolution direct numerical simulation of turbulence: Reynolds number dependence of one-point velocity gradients statistics," J. Fluid Mech. **592**, 335 (2007).
[30] R. S. Rogallo, "Numerical experiments in homogeneous turbulence," NASA Report No. TM 81315, 1981.
[31] P. E. Hamlington, J. Schumacher, and W. J. A. Dahm, "Local and nonlocal strain rate fields and vorticity alignment in turbulent flows," Phys. Rev. E **77**, 026303 (2008).
[32] P. Vedula and P. K. Yeung, "Similarity scaling of acceleration and pressure statistics in numerical simulations of isotropic turbulence," Phys. Fluids **11**, 1208 (1999).
[33] P. K. Yeung, S. Xu, and K. R. Sreenivasan, "Schmidt number effects on turbulent transport with uniform mean scalar gradient," Phys. Fluids **14**, 4178 (2002).
[34] A. N. Kolmogorov, "A refinement of previous hypothesis concerning the local structure of turbulence in viscous incompressible fluid at high Reynolds number," J. Fluid Mech. **13**, 82 (1962).
[35] G. Paladin and A. Vulpiani, "Degrees of freedom of turbulence," Phys. Rev. A **35**, 1971 (1987).
[36] G. Stolovitzky and K. R. Sreenivasan, "Scaling of structure functions," Phys. Rev. E **48**, R33 (1993).
[37] C. Meneveau and K. R. Sreenivasan, "Simple multifractal cascade model for fully developed turbulence," Phys. Rev. Lett. **59**, 1424 (1987).
[38] I. Hosokawa, "Turbulence models and probability distributions of dissipation and relevant quantities in isotropic turbulence," Phys. Rev. Lett. **66**, 1054 (1991).
[39] C. Meneveau and K. R. Sreenivasan, "The multifractal nature of turbulent energy dissipation," J. Fluid Mech. **224**, 429 (1991).
[40] A. Bershadskii, E. Kit, and A. Tsinober, "On universality of geometrical invariants in turbulence—Experimental results," Phys. Fluids A **5**, 1523 (1993).
[41] T. Zhou, R. A. Antonia, and L. P. Chua, "Flow and Reynolds number dependencies of one-dimensional vorticity fluctuations," J. Turbul. **6**, 28 (2005).
[42] G. R. Ruetsch and M. R. Maxey, "Small-scale features of vorticity and passive scalar fields in homogeneous turbulence," Phys. Fluids A **3**, 1587 (1991).
[43] A. N. Karpetis and R. S. Barlow, "Measurements of scalar dissipation in a turbulent piloted methane/air jet flame," Proc. Combust. Inst. **29**, 1929 (2002).
[44] M. Nelkin, "Inertial range scaling of intense events in turbulence," Phys. Rev. E **52**, R4610 (1995).
[45] Z.-S. She and E. Leveque, "Universal scaling laws in fully developed turbulence," Phys. Rev. Lett. **72**, 336 (1994).
[46] V. Yakhot, "Probability densities in strong turbulence," Physica D **215**, 166 (2006).
[47] R. Benzi, L. Biferale, G. Paladin, A. Vulpiani, and M. Vergassola, "Multifractality in the statistics of the velocity gradients in turbulence," Phys. Rev. Lett. **67**, 2299 (1991).
[48] R. A. Antonia, T. Zhou, and Y. Zhu, "Three-component vorticity measurements in a turbulent grid," J. Fluid Mech. **374**, 29 (1998).
[49] S. Lee and C. Lee, "Intermittency of acceleration in isotropic turbulence," Phys. Rev. E **71**, 056310 (2005).
[50] N. Mordant, E. Lévêque, and J. F. Pinton, "Experimental and numerical study of the Lagrangian dynamics of high Reynolds turbulence," New J. Phys. **6**, 116 (2004).
[51] P. K. Yeung, S. B. Pope, E. A. Kurth, and A. G. Lamorgese, "Lagrangian conditional statistics, acceleration and local relative motion in numerically simulated isotropic turbulence," J. Fluid Mech. **582**, 399 (2007).
[52] Z. S. She, E. Jackson, and S. A. Orszag, "Structure and dynamics of homogeneous turbulence—models and simulations," Proc. R. Soc. London, Ser. A **434**, 101 (1991).
[53] J. Jiménez, A. A. Wray, P. G. Saffman, and R. S. Rogallo, "The structure of intense vorticity in isotropic turbulence," J. Fluid Mech. **255**, 65 (1993).
[54] F. Moisy and J. Jiménez, "Geometry and clustering of intense structures in

isotropic turbulence," J. Fluid Mech. **513**, 111 (2004).
[55]B. Dhruva, Y. Tsuji, and K. R. Sreenivasan, "Transverse structure functions in high-Reynolds-number turbulence," Phys. Rev. E **56**, R4928 (1997).
[56]P. K. Yeung and Y. Zhou, "On the universality of the Kolmogorov constant in numerical simulations of turbulence," Phys. Rev. E **56**, 1746 (1997).
[57]S. B. Pope, *Turbulent Flows* (Cambridge University Press, Cambridge, 2000).